Research article

Numerical simulation study on heat performance and pressure loss of solar air heater with sinusoidal baffles

Xiaolong Wang[1], Lingning Zhang[2], Yuan Chang[3], Yang Song[1] and Liang Wang[2],*

[1] School of Energy and Machinery, Dezhou University, Dezhou 253023, China
[2] School of Thermal Engineering, Shandong Jianzhu University, Jinan 250101, China
[3] School of Art, Shandong Management University, Jinan 250101, China

* **Correspondence:** Email: wanglianglre@163.com; Tel: +86-15662717936.

Abstract: Heat performance and internal pressure loss are important reference standards in solar air heaters (SAH). In order to solve the problem of too large a pressure loss in SAH, an innovative SAH with sinusoidal baffles was proposed on the basis of folded baffle and semi-circular baffle air heaters. A computational fluid dynamics (CFD) simulation calculation was performed for the SAH with sinusoidal baffles, and the relevant parameters, such as the heat collection efficiency and the pressure loss, were analyzed. The results showed that the sinusoidal baffle had a better heat collection performance and a smaller pressure loss compared to the folded baffle and the semi-circular baffle. A sinusoidal baffle can further improve the thermal performance of SAH. The simulation calculation of wave lengths for sinusoidal baffles revealed that when the wavelength value was 200 mm, the SAH had the best heat collection effect, and the heat collection efficiency was 64.49%. On the basis of determining the wavelength, the wave height of the sinusoidal baffle was studied. When the wave height was 30 mm, the minimum pressure loss of the SAH was 17.51 Pa, and the maximum heat collection efficiency was 64.91%. Analyses and research on the Reynolds number of the air inlet showed that as the Reynolds number increased, the collection efficiency and internal pressure loss gradually increased, while the outlet temperature decreased. The curve fitting of the imported Reynolds number and the pressure loss showed that the accuracy of pressure loss fitting curve is 0.997. Research on a double-layer SAH showed that the cross different inlet (CDI) had the best collector performance. This research has a high practicality and can provide a theoretical basis for winter air heating.

Nomenclature: a: spectral absorption coefficient; c: specific heat capacity; d: equivalent diameter(m); F: volume force(N); K: turbulent energy(J); m: mass flow(kg·s^{-1}); n: spectral refractive index; p: pressure(Pa); $\boldsymbol{r}$: direction vector; S: source term; s: length of air passage(m); $\boldsymbol{s}$: direction vector; T: temperature(K); t: time(s); u: velocity of x axis(m·s^{-1}); V: specific volume(m^3·kg^{-1}); v: velocity of y axis(m·s^{-1}); w: velocity of z axis(m·s^{-1});

Greek letters: α: equation coefficient; τ: time(s); ρ: density(kg·(m^3)$^{-1}$); ε: turbulent dissipation; σ: Stephen Boltzmann constant; μ: dynamic viscosity(Pa·s); v: kinematic viscosity(m^2·s^{-1}); Ω: solid angle of light source emission; η: collector efficiency(%); φ: scattering phase coefficient of condensed phase;

Subscripts: A_c: endothermic area(m^2); C_k: model coefficient; C_p: specific heat capacity at constant pressure(J·(kg·k)$^{-1}$); C_ε: empirical coefficient; $C_{1\varepsilon}$: empirical coefficient; $C_{2\varepsilon}$: empirical coefficient; $C_{3\varepsilon}$: empirical coefficient; d_α: dimensionless number; G_T: absorbing radiation(W·(m^2)$^{-1}$); I_λ: radiation intensity(W·sr^{-1}); P_b: buoyancy generating term; P_k: velocity generating term; S_φ: source term; T_0: inlet temperature(K); T_i: outlet temperature(K); u_i, u_j: velocity of vector direction(m·s^{-1}); μ_t: dynamic viscosity of time(Pa·s); v_t: kinematic viscosity of time(m^2·s^{-1}); Y_k: fluctuating expansion coefficient; σ_ε: dissipation rate Prandtl; σ_s: spectral scattering coefficient

1. Introduction

A solar air heater (SAH) is a cost-effective solar device that can be constructed using readily available materials, thus minimizing fabrication expenses [1]. A SAH heats the air by absorbing solar radiation, so as to achieve the purpose of indoor heating and drying agricultural products [2]. The flat plate collector consists of an absorb plate covered by a transparent glass cover, copper tubes, and an aluminum back plate [3]. Additionally, solar energy is used in the direction of energy storage, such as storing solar energy to heat buildings [4], or when the spiral tube collector is filled with glycerol and paraffin for energy storage [5]. Phase change materials (PCM) are added to the air collector to improve the operation cycle and the collection efficiency of the heater [6]. The method of improving the traditional PCM can change the extended surface structure by using porous materials, metal foam, or high light thermal materials [7].

Scholars have extensively researched the thermal performance of SAH, including adding double channels [8] and spiral flow channels [9] to an SAH to improve its heat collection performance. Some scholars have updated the heat absorb plate by designing a heat sink [10], a parabolic surface [11], and a spherical heat absorb plate [12].

Many researchers began to achieve the goal of improving the collection efficiency by improving the structure of the air heater, thus optimizing the structure of the SAH. This includes using slotted perforated corrugated plates [13] and triangular plates [14]. Some scholars have added parabolic grooves [15] and louvers [16] to the heat absorb plates to improve the heat collection performance of the SAH.

Other scholars have made new SAH by optimizing the internal structure based on the traditional flat panel SAH; this includes adding circular fins [17], rough fins [18], and rectangular fins [19] into

the SAH. Together, these studies can improve the heat absorption efficiency of the heat absorbing plate, thus enhancing the heat collection performance of SAH. In order to improve the heat collection efficiency of a SAH, researchers introduced closed-loop pulsating heat pipes [20], C-shaped fins [21], spiral fins [22], V-shaped fins [23], and porous media fins [24] into the heat absorb plate. Additionally, some scholars have studied a baffle type SAH, such as folded baffles [25], spiral baffles [26], and hollow semi-circular [27] SAH. The results indicate that the internal air temperature was higher than that of a traditional flat plate heater. The collection efficiency has also been greatly improved.

Jia [28] analyzed and studied the number of baffles for a spiral SAH, and the results showed that the optimal structure is a spiral SAH with two longitudinal baffles. Some scholars have combined the heat absorb plate with a PCM. Mahamad [29] equipped the wave shaped corrugated solar air collector with a PCM, and found that the energy efficiency increased by about 20% when equipped with a PCM. Magda [30] added a PCM to the interior of the flat panel solar collector, and showed that the temperature rise could reach 31% compared to the standard SAH.

In previous studies on baffle SAH, the main focus was on improving the collection efficiency and daily utilization rate of SAH. The air pressure loss inside the SAH is also an important factor, and the baffle type SAH can certainly improve the heat utilization and the air flow. The pressure loss in the folded baffle SAH [25] is significant, and the semi-circular baffle SAH [31] can reduce the pressure loss, though the thermal utilization rate will decrease. On the basis of these two types of baffle SAH, a sine baffle is added to the SAH in this study. The purpose is to improve the thermal utilization of the SAH and reduce the internal pressure loss by studying the parameters of sinusoidal baffles. The research investigates the impact of varying the wavelength and the wave height of the sinusoidal baffles on the outlet temperature, the collection efficiency, and the pressure loss. Additionally, the study determines the optimal inlet Reynolds number by assessing its influence on its thermal performance. Finally, this research aims to reveal the factors that affects the thermal utilization and pressure loss of sinusoidal baffles SAH. The practicality of sinusoidal baffles SAH lies in its ability to improve the heat utilization, reduce the pressure loss, and provide a theoretical basis for using air heating in winter, thus ensuring that the temperature of indoor air heating is maintained at an appropriate temperature. The innovation of this study is the addition of a sinusoidal baffle in SAH and its investigation.

2. Physical model and boundary setting

2.1. Sinusoidal baffles SAH model

The physical model of the heater is shown in Figure 1. The Fluent software is used to build the model. The overall height of the SAH is 80 mm and the air flow passage height is 50 mm. The SAH has eight baffle plates, and the cover plate is composed of polycarbonate (PC), which has a good light transmittance. The thickness of the PC cover plate is 4 mm. Due to the high thermal conductivity and low price of aluminum, when heat flows through the aluminum surface, it immediately absorbs heat. Therefore, the material for the heat absorb plate is aluminum. The heat absorb plate and baffle plate are both made of aluminum, with a thickness of 3 mm. The area of the air inlet and outlet is 0.0045 m^2. The bottom of the SAH is the insulation layer, which is mainly composed of asbestos rock wool, with a thickness of 30 mm. Air bends along the channel composed

of the sinusoidal baffle, the PC cover plate, and the insulation layer in the SAH. Due to the high temperature of the absorb plate and baffle plates, the air temperature rises. The specific dimensions of the SAH components are shown in Table 1.

Table 1. Structural parameters of sinusoidal baffles SAH.

Name	Length/mm	Width/mm	Height/mm	Material	Absorptivity	Transmittance
PC cover plate	2060	1000	4	Polycarbonate	0.021	0.9
Absorb plate	2060	1000	3	Aluminum-nitrogen-aluminum	0.94	/
Insulation layer	2060	1000	30	Rock wool	/	/
Inlet/Outlet	150	30	/	/	/	/
Baffle	800	50	3	Aluminum-nitrogen-aluminum	0.94	
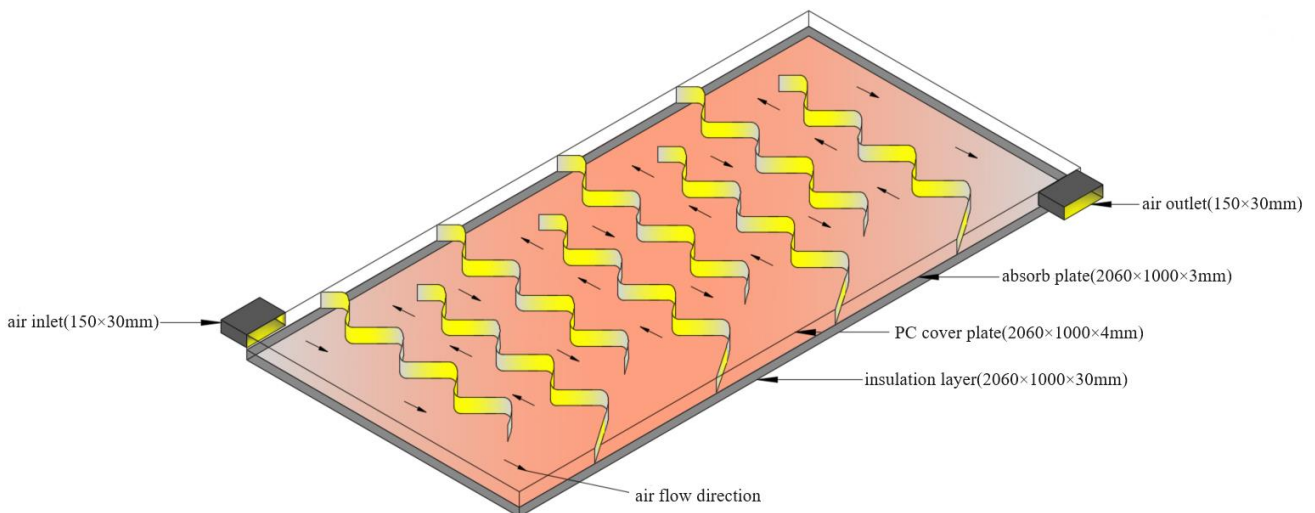
Figure 1. Physical model of SAH with sinusoidal baffles.

2.2. Model selection and equations
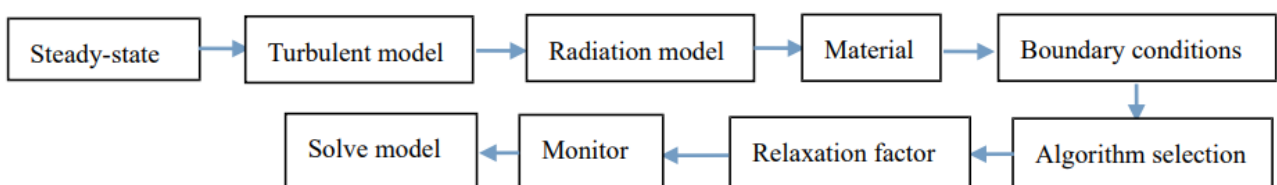
Figure 2. Model simulation solution process.

The model process is shown in Figure 2. The entire process of establishing and calculating

models is carried out using the Fluent software. First, the steady-state calculations are selected in the model. The equations in the model include the continuity equation, the momentum equation, and the energy equation [30,31]:

$$\frac{\partial \rho}{\partial \tau} + \frac{\partial (\rho u)}{\partial x} + \frac{\partial (\rho v)}{\partial y} + \frac{\partial (\rho w)}{\partial z} = 0 \tag{1}$$

In Eq 1, ρ is the density (kg/m^3), τ is the time (s) and u,v,w are the velocity component (m/s).

$$\rho \frac{DV}{D\tau} = F - \nabla p + \mu \nabla^2 V \tag{2}$$

V is the specific volume (m^3/kg) τ is time (s), F is the volume force (N), p is the pressure (pa), and μ is the dynamic viscosity (pa·s).

$$\frac{\partial T}{\partial \tau} + (u\frac{\partial T}{\partial x} + v\frac{\partial T}{\partial y} + w\frac{\partial T}{\partial z}) = \frac{\lambda}{\rho c} \cdot (\frac{\partial^2 T}{\partial x^2} + \frac{\partial^2 T}{\partial y^2} + \frac{\partial^2 T}{\partial z^2}) + S \tag{3}$$

T is the temperature (K), λ is the thermal conductivity (W/m·K), c is the specific heat capacity (J/kg·K), and S is the source.

$$Re = \frac{ud}{\upsilon} \tag{4}$$

Re is the Reynolds number, d is the equivalent diameter (m), and v is the kinematic viscosity (m^2/s).

The Reynolds number of the air inlet calculated by Eq (4) is 0.57×10^4. The realizable K-ε model is selected to better calculate the process of complex fluid flow. Moreover, the realizable K-ε model can not only improve the computational accuracy, but also add a formula for the fluid viscosity calculation on the basis of the renormalization group K-ε (RNG K-ε) [31]. This model is suitable for a wide range of flow types, including rotational uniform shear flow, free flow, and boundary layer flow. The simulation results of the above flow processes are better than those of the standard K-ε model. Especially, the realizable K-ε model can simulate both circular jets and flat jets, and can provide good jet expansion angles. According to the references [25,26,28,31], it is known that when air flows in the SAH, there is a turbulent boundary layer inside, and there is a medium viscosity during the turbulent flow. Moreover, when air flows on this baffle, there are vortices inside the flow field that need to consider the near wall area. Therefore, a realizable K-ε model is chosen in this research.

The discrete ordinates (DO) model is selected on the radiation model, as the DO model can solve all radiation problems. In the references [28,31], the DO model is also used for the solar radiation model problem. The model in the define of the solver is selected, followed by selecting the radiation model and the DO model. Then, the longitude, dimension, and time zone in the global position of the sun calculator are selected, followed by the month, date, hour, and minute in the start date and time. Next, the East and North direction vectors in grid orientation are chosen. The direction of the SAH is determined by setting the position of the coordinate axis. In the pressure-velocity

coupling of Fluent, the SIMPLE algorithm is the default setting and belongs to a type of pressure correction method, which is suitable for steady-state calculations. SIMPLE can provide more accurate calculation results when air undergoes a complex flow in the SAH. SIMPLE algorithm is also used for pressure-velocity coupling selection in solution control in solvers.

The realizable K-ε equation is as follwos [32]:

$$\frac{\partial}{\partial t}(\rho K) + \frac{\partial}{\partial x_j}(\rho K u_j) = \frac{\partial}{\partial x_j}[(\mu + \frac{\mu_t}{\sigma_k})\frac{\partial K}{\partial x_j}] + P_k + P_b - \rho\varepsilon - Y_k + S_k \tag{5}$$

K is the turbulent kinetic energy (J), μ_j is the direction of the velocity component j, μ_t is the unsteady dynamic viscosity (pa·s), σ_k is the turbulent Prandtl number ($\sigma_k = 1.0$), P_k is the turbulent kinetic energy caused by the average velocity gradient (J), P_b is the turbulent kinetic energy caused by buoyancy (J), ε is the turbulent dissipation rate, Y_k is the influence of the compressible turbulent pulsation expansion on dissipation rate, and S_k is the turbulent energy source.

$$\frac{\partial}{\partial t}(\rho\varepsilon) + \frac{\partial}{\partial x_j}(\rho\varepsilon u_j) = \frac{\partial}{\partial x_j}[(\mu + \frac{\mu_t}{\sigma_\varepsilon})\frac{\partial\varepsilon}{\partial x_j}] + \rho C_{1\varepsilon}S_\varepsilon - \rho C_{2\varepsilon}\frac{\varepsilon^2}{K + \sqrt{v\varepsilon}} + C_{1\varepsilon}\frac{\varepsilon}{K}C_{3\varepsilon}P_b + S_k \tag{6}$$

$C_{1\varepsilon}$ is constant ($C_{1\varepsilon} = 1.44$), $C_{2\varepsilon}$ is constant ($C_{2\varepsilon} = 1.92$), $C_{3\varepsilon}$ is constant ($C_{3\varepsilon} = 0.09$), and S_k is the turbulent dissipation rate source.

The model adopts a two-equation model and is solved using a standard-wall function. To ensure the accuracy of this model calculation, it is necessary to ensure that y+ > 15. The boundary layer can be divided into three types based on the value of y+: a viscous bottom layer (0 < y+ < 5), a buffer layer (5 < y+ < 30), and a fully turbulent layer (y+ > 30). The air flow process belongs to a turbulent flow, with a turbulent boundary layer, and the solution process uses a near wall function. Therefore, the value of y+ used is 30 < y+ < 60.

The DO equation is as follows [32]:

$$\frac{dI_\lambda(\mathbf{r},\ \mathbf{s})}{ds} + (a + \sigma_s)\ dI_\lambda(\mathbf{r},\ \mathbf{s}) = an^2\frac{\sigma T^4}{\pi} + \frac{\sigma_s}{4\pi}\int_0^{4\pi}I_\lambda(\mathbf{r},\ \mathbf{s})\ \Phi\ (\mathbf{s},\ \mathbf{s})\ d\Omega \tag{7}$$

I_λ is solar radiation intensity (W/m^2), s is the air channel length (m), $\mathbf{r}$ is the position vector, $\mathbf{s}$ is the direction vector, a is the spectral absorption coefficient, σ_s is the spectral scattering coefficient, n is the spectral refractive coefficient, σ is the Stephen Boltzmann constant ($\sigma = 5.67 \times 10^{-8}$ W/m^2·K^4), ϕ is the scattering phase function, and Ω is the light source emission solid angle,°.

All the control equations mentioned above are solved using the Fluent software. The corresponding conditional parameters are set in the Fluent solver, such as the air inlet velocity, the temperature, and the ambient temperature. The solver will calculate the corresponding air outlet temperature and the internal pressure loss based on the control equations.

The efficiency of the heat collector calculation formula is as follows [31]:

$$\eta = \frac{mC_p(T_0 - T_i)}{A_c G_T} \tag{8}$$

η is the heat collection efficiency (%), m is the mass flow (kg/s), c_p is the specific heat capacity

at a constant pressure (kg/m·K), T_0 is the inlet temperature (K), T_i is the outlet temperature (K), A_c is the endothermic area (m^2), and G_T is the absorbing radiation (W/m^2).

2.3. Boundary condition and validation

The simulation conditions of this study are consistent with the reference literature [31] and can serve as the basis for subsequent comparative studies. The numerical calculation is mainly aimed at the air outlet temperature, which means that after the air flow process reaches stability, the calculation process is a steady-state calculation. The model in the reference literature [31] is a semi-circular baffle SAH. The dimensions are the same as the model in this study, though the difference lies in the type of baffle. The boundary condition of the PC cover plate is set as a mixed boundary condition (including thermal convection and thermal radiation). The boundary condition of the absorb plate and the sinusoidal baffles is set as a couple boundary condition (the boundary conditions caused by the interaction between different physical fields). The air inlet and outlet are set as the velocity inlet and the pressure outlet boundary conditions, respectively. The air inlet velocity is set to 2 m/s, the turbulent intensity is 5%, and the hydraulic diameter is 0.005 m. The external ambient temperature is set to 274 K, and the air inlet temperature is set to 278 K. These conditions are consistent with [31].

The calculation assumptions for this simulation are as follows:

(1) The heat loss of the insulation layer is ignored;

(2) The parameters of air are constant physical properties;

(3) The transmittance of the PC board is considered to be 0.9 and the absorption rate of absorption board is considered to be 0.94.

Before conducting calculations, it is necessary to verify the grid.

The pre-processor Gambit function of Fluent is used to perform grid partitioning on the model. The mesh division of the model is shown in Figure 3(a). The reason for choosing an unstructured mesh is because this model includes a sinusoidal baffle, which belongs to a complex geometric model. In computing complex geometric models, unstructured meshes have a better stability and accuracy; therefore, unstructured meshes are typically used. In order to accurately capture the flow of air in the channel, it is necessary to use a denser grid at the air channel. Therefore, the number of grids in the flow channel is relatively dense, while the grids in other areas are relatively sparse, which can improve the calculation velocity. The grid independence validation of model is shown in Figure 3(b), which uses pressure in the momentum equation as the reference quantity. As the number of grids increases, the internal pressure gradually decreases. When grid number is 6.4×10^5, there is little change in the internal pressure. Therefore, the number of grids calculated by the model is 6.4×10^5.

(a) Model meshing diagram.
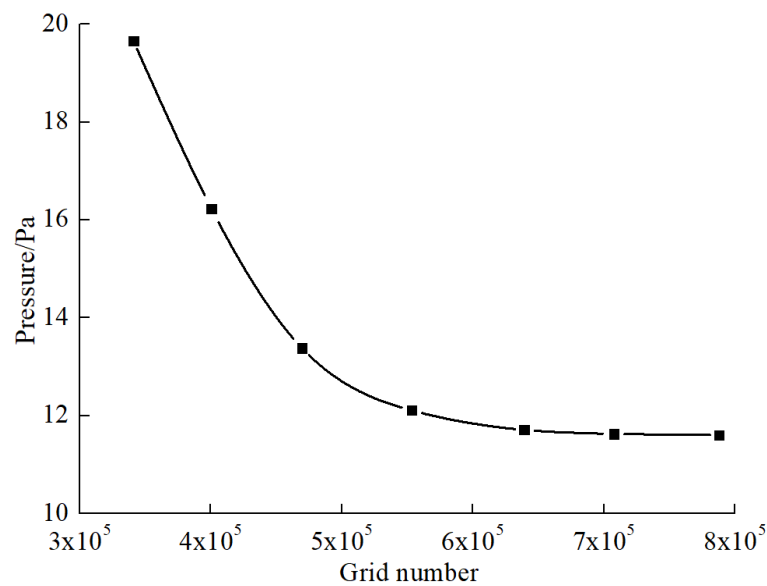
(b) Grid independence test.

Figure 3. Model meshing and independence test.

## 2.4. Calculation accuracy verification

It is necessary to validate the accuracy of the chosen calculation methodology. As seen in Figure 4(a), the calculation approach employed in this investigation aligns with the one documented in the referenced literature [31]. The x-axis time unit in Figure 4(a) is hours. Due to the different solar radiation at each moment, simulation calculations need to be conducted separately for different time periods. The scrutiny of deviations in these references revealed that experimental data cited from reference [32] exhibited relatively elevated outlet temperatures. The reason for this situation is that the air is transported into the SAH by the fan, which consumes electrical energy and converts it into thermal energy. There is frictional heat generation at the inlet of the air. Additionally, the ambient temperature increase is a contributing factor. Upon the meticulous comparative analysis, it becomes evident that the simulated calculation results exhibit consistent correspondence with the

experimental data. According to the experimental deviation bar analysis in Figure 4(b), the deviation between the average value and the measured data of the experimental results is very small. This compellingly attests to the precision and reliability of the selected calculation method, thus warranting its application for the calculations and subsequent analysis within this study.
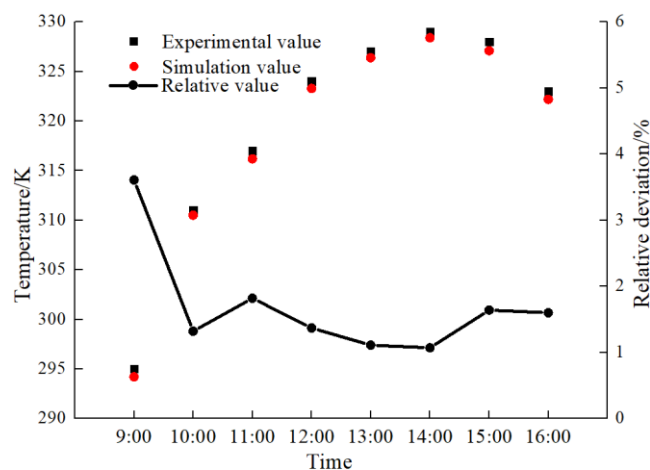
(a) Comparison between experimental and calculated.
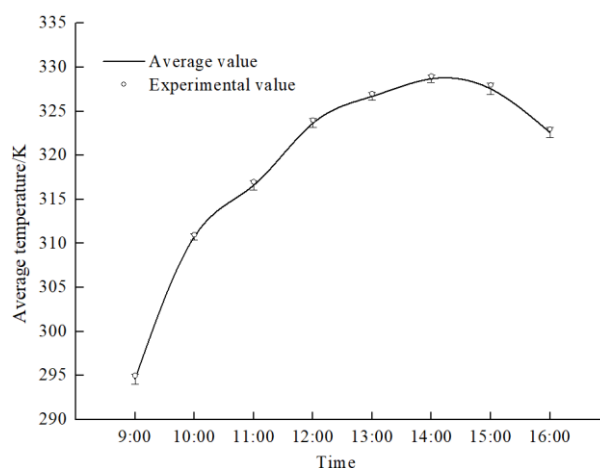
(b) Average value and error bar.

Figure 4. Comparison of experimental and simulated air outlet temperature.

3. Results and discussion of Sinusoidal baffles SAH

3.1. Comparative calculation

3.1.1. Comparison with folded baffle collector

In order to highlight the advantages of the SAH with sinusoidal baffles, it is necessary to compare the data with previous studies. First, the SAH with sinusoidal baffles is compared with the folded baffle SAH [25]. The number, space, and height of baffles of the two SAHs are controlled to

be consistent. The number of baffles is 6, the space of the baffles is 500 mm, and the wave height and wavelength of the sinusoidal baffle are 200 mm. The length of the two models is slightly different, in which the total length of the folded baffle collector is 3327.6 mm and the total length of the SAH with sinusoidal baffles is 3153.6 mm. The control air inlet temperature is 278 K and the ambient temperature is 274 K. The air inlet velocity is 2 m/s since the air inlet is a rectangular channel, and the equivalent diameter of the inlet is 0.05 m.

A scrutiny of the numerical deviations in these references reveals that the experimental data cited from reference [33] exhibited relatively elevated outlet temperatures, primarily due to frictional heating arising from the inlet and outlet air in the experimental setup. Upon a meticulous comparative analysis, it becomes evident that the simulated calculation results exhibit a consistent correspondence with the experimental data. Notably, the maximal deviation observed between the two data does not surpass 5%. This compellingly attests to the precision and reliability of the selected calculation method, thus warranting its application for the calculations and subsequent analysis within this study.

The calculation results of two different models are shown in Table 2. The temperature and velocity distribution of the SAH with sinusoidal baffles are shown in Figure 5.

Table 2. Comparative data of the two SAHs.

Collector type	Outlet temperature/K	Heat collection efficiency/%	Pressure loss/Pa
Folded baffle [25]	361.4	50.10	14.74
Sinusoidal baffle	361.9	53.44	6.71
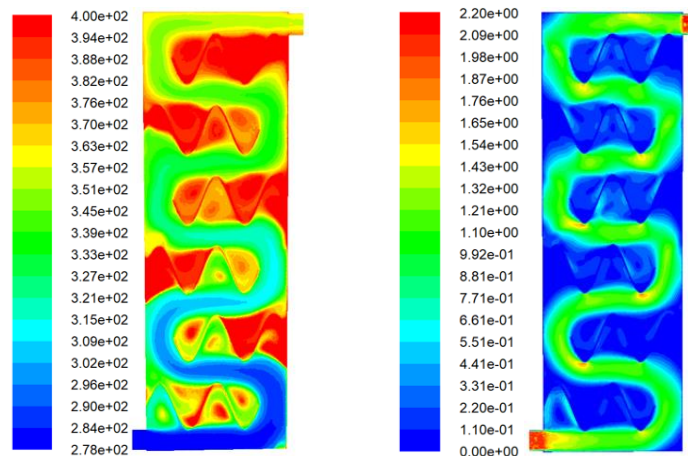
(a) Temperature distribution.   (b) Velocity distribution.

Figure 5. SAH with sinusoidal baffles comparison calculation distribution.

The comparative data of the two SAHs is presented in Table 2. As can be seen from the data in Table 2, the outlet temperature of the two SAHs have little differences. In reference [25], the heat collection efficiency of the SAH was 50.1%, and the internal air pressure loss was about 14.74 Pa. The collection efficiency of the sinusoidal baffle SAH is 23.44%. It can be seen that the SAHs with sinusoidal baffles has not only a higher heat collection efficiency, but also has a lower pressure loss. The air inlet velocity used in the comparative study is 2 m/s. According to reference [25], as the air

inlet velocity increases, the collection efficiency and pressure loss of the SAH will also increase. Therefore, the comparison shows that the SAH with sinusoidal baffles has greater advantages. This SAH can greatly reduce the fan losses and improve the thermal utilization efficiency of solar energy.

3.1.2. Comparison with semicircular baffle collector

As studied by Wang (2022) [31], a comparison between the performance of the SAH equipped with sinusoidal baffles and those with semicircular baffles [28] is imperative. It is noteworthy that both configurations maintain a consistent collector length of 2060 mm and a baffle spacing of 300 mm. The sinusoidal baffle's wave height and wavelength are set at 20 mm and 80 mm, respectively, thus mirroring the dimensions of the semicircular baffle. Additionally, the inlet air parameters align with those previously described in the calculations. For reference, detailed results and findings are presented in Figure 6 and Table 3.

Table 3. Comparative results of two collector parameters.

Collector type	Outlet temperature/K	Heat collection efficiency/%	Pressure loss/Pa
Semicircular baffle [31]	334.0	54.7	15.30
Sinusoidal baffle	343.42	63.48	11.17
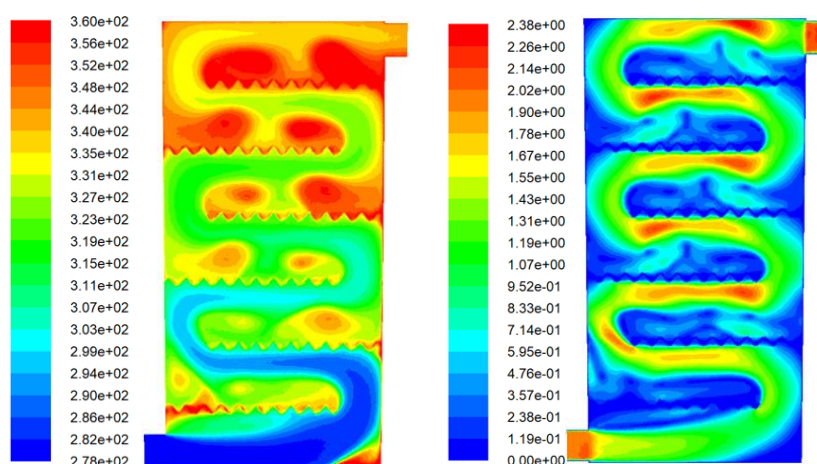
(a) Temperature distribution.   (b) Velocity distribution.

Figure 6. SAHs with sinusoidal baffles comparison calculation distribution.

According to the data in Table 3, under the same inlet conditions, the outlet temperature and heat collection efficiency of the SAH with sinusoidal baffles are higher than those of a semicircular baffle SAH, though the pressure loss is smaller. The collection efficiency of the semi-circular baffle SAH in reference [31] was 54.7%, and the internal pressure loss was 15.3 Pa. The collection efficiency of the sinusoidal baffle SAH is about 63.48%, and the internal pressure loss is 11.17 Pa. Due to the small difference in the flow state of air between these two types of SAHs, the pressure loss is not significantly different. Due to the large area of the sinusoidal baffle, the heat gain of the air increases, thus resulting in a higher outlet temperature and a higher heat collection efficiency. Moreover, as the air inlet velocity increases, the collection efficiency will further increase. From this,

it can be seen that the sinusoidal baffle SAH can provide a higher air indoor temperature in the winter, making it more suitable for indoor air heating in the winter. Therefore, a SAH with sinusoidal baffles has a high research value. This kind of collector needs to be deeply studied and explored.

3.2. Influence of sinusoidal wavelength on parameters

The wavelength and height of sinusoidal ripples can significantly influence the airflow patterns. To comprehensively understand their specific impacts, an in-depth analysis is imperative. We commence this exploration by examining the effects of varying wavelengths on key air heat transfer parameters. We consider different wavelength values while maintaining a consistent wave height of 50 mm for the sinusoidal baffle: 100 mm, 200 mm, 400 mm, and 800 mm. The control air's inlet temperature is set at 278 K, the ambient temperature at 274 K, and the air inlet's Reynolds number at 0.57×10^4. These conditions are employed in the assessment of the SAH equipped with sinusoidal baffles with varying wavelengths. Detailed calculation data and results can be found in Figure 7.
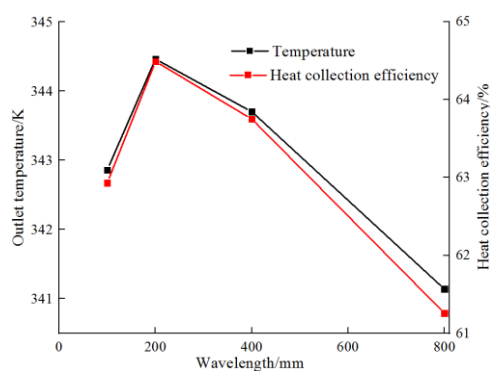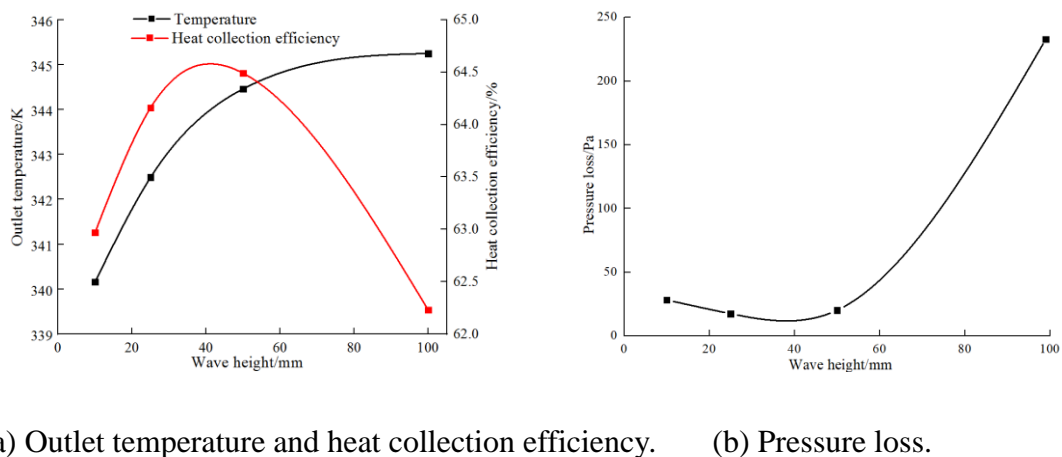

Figure 7. Parameter calculation results.

As can be seen from the curve in Figure 7, the change trend of the outlet temperature and the heat collection efficiency is the same, both rising first and then falling. This situation shows that the wavelength of the sinusoidal baffle affects the flow process of air on the sinusoidal baffle. Due to the convection heat transfer between the PC cover plate and the air, there is direct contact heat conduction between the PC cover plate and the sinusoidal baffle. Therefore, the heat gain of air belongs to the role of the comprehensive factors. The maximum value of the outlet temperature and the heat collection efficiency occurs when the wavelength value is 200 mm. The pressure losses at the four different wavelengths are 19.13 Pa, 20.32 Pa, 19.11 Pa, and 27.15 Pa, respectively. When the wavelength value is 400 mm, the pressure loss is the smallest; when the wavelength value is 200 mm, the difference of pressure loss is 1.21 Pa. This pressure loss deviation shows that the pressure loss caused by the two wavelength values is not different. Considering the changes of the outlet temperature, the heat collection efficiency, and the pressure loss parameters, the wavelength of 200 mm is selected as the best wavelength for further research.

3.3. Influence of sinusoidal wave height on parameters

Through the above calculation and research, it is found that when the wavelength value is selected as 200 mm, the comprehensive parameters of collector are superior. The sinusoidal baffle wave height will also affect the air flow process. The sinusoidal baffle wave height values are set as 10 mm, 25 mm, and 100 mm, respectively, and the heat transfer process of the SAH with sinusoidal baffles are calculated with different wave height values under the premise of keeping the air inlet parameters and environmental parameters unchanged. The specific calculation result is shown in Figure 8.

(a) Outlet temperature and heat collection efficiency.   (b) Pressure loss.

**Figure 8.** Parameter calculation results.

As depicted in the data curve in Figure 8, it is evident that the outlet temperature of the air exhibits a gradual increase. This phenomenon can be attributed to variations in the wave height of the sinusoidal baffle, which, in turn, leads to different total lengths of the collector. Importantly, the space between the sinusoidal baffles remains constant. As the wave height increases, the collector's length grows, resulting in a gradual rise in air heat gain, and consequently an increase in the outlet temperature of the air. Notably, the heat collection efficiency follows an initial increase and then decreases. Conversely, the pressure loss experiences an initial decline followed by an increase.

The reasons for the changes of heat collection efficiency and pressure loss are subsequently analyzed. When the length of the SAH becomes longer, the heat gain of air and the outlet temperature rise; however, the overall heat absorption of the SAH also increases, so the SAH efficiency curve will change. Moreover, when the wave height of the sinusoidal baffle increases, the flow of air on the sinusoidal corrugated baffle will be blocked, resulting in air that will not sweep over the sinusoidal baffle, but directly flow between the baffles. This causes the air to flow through smaller places, thus resulting in increased pressure loss.

By observing the changes of the heat collection efficiency curve and the pressure loss curve, it can be seen that there is a specific wave height value, which makes the heat collection efficiency the highest and the pressure loss the smallest. Therefore, in order to select the best wave height, further calculations and research are needed.

The wave heights of the sinusoidal baffle are set as 20 mm, 30 mm, 35 mm, 40 mm, and 45 mm. The SAH with sinusoidal baffles with these wave heights is calculated and studied, and compared

with the working conditions with wave heights of 25 mm and 50 mm. The specific comparison data curve is shown in Figure 9.
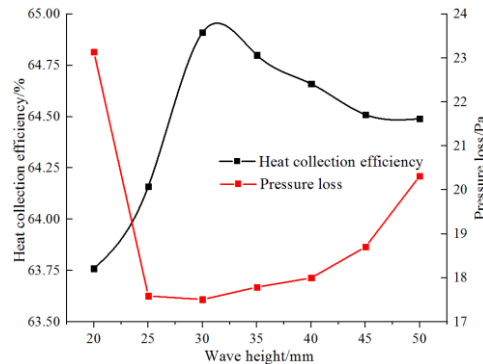
Figure 9. Calculation results of different wave height data.

The data trend in Figure 9 reveals the specific wave height, 30 mm in particular, which maximizes the heat collection efficiency while minimizing the pressure loss. Under these conditions, the heat collection efficiency reaches 64.91%, alongside a pressure loss of 17.51 Pa. This suggests that a wave height of 30 mm ensures the most comprehensive and uniform contact between air and the baffle. However, as the wave height further increases, the air no longer fully interacts with the sinusoidal baffle, but instead flows directly through the channel along a straight path, leading to an increased pressure loss.

Table 4. Turbulence calculation data.

Wave height/mm	Turbulent kinetic energy/$(m^2 \cdot s^{-2})$	Turbulent intensity/%	Turbulent dissipation rate/$(m^2 \cdot s^{-3})$
20	0.016	9.303	0.217
25	0.015	9.045	0.197
30	0.015	9.03	0.195
35	0.015	9.051	0.195
40	0.017	9.506	0.218
45	0.019	9.966	0.251
50	0.02	10.233	0.259

Therefore, when the wavelength is 200 mm, the wave height value of 30 mm is the most appropriate.

3.4. Influence of inlet Reynolds number on parameters

According to previous research, the optimal ripple size of the SAH with sinusoidal baffles has a wavelength of 200 mm and a wave height of 30 mm. Therefore, the effects of different air inlet Reynolds numbers on the SAH parameters need to be calculated and studied. On the premise that the air inlet temperature is 278 K and the ambient temperature is 274 K, the air inlet velocity is adjusted to 1 m/s, 1.5 m/s, 2.5 m/s, 3 m/s, and 3.5 m/s, and the corresponding Reynolds numbers are 0.29×10^4, 0.43×10^4, 0.71×10^4, 0.86×10^4, and 1×10^4, respectively.
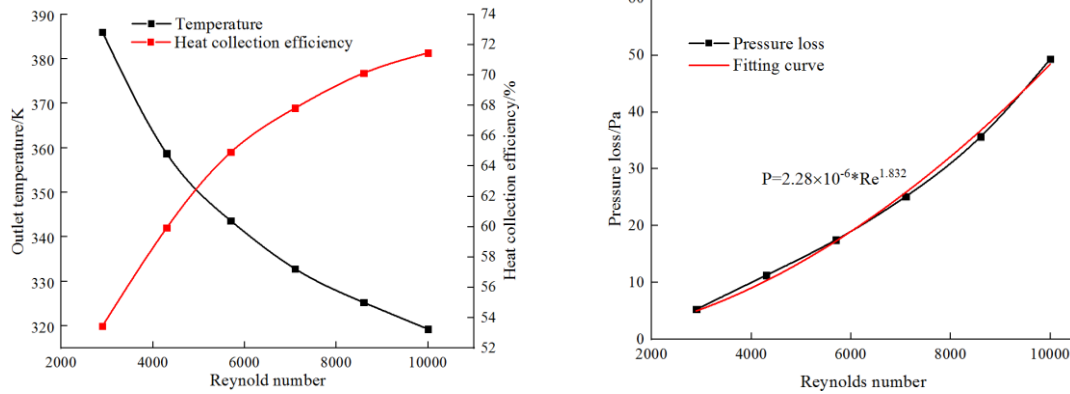
(a) Outlet temperature and heat collection efficiency.　　　(b) Pressure loss.

Figure 10. Heat collection efficiency and pressure loss of different inlet Reynolds numbers.
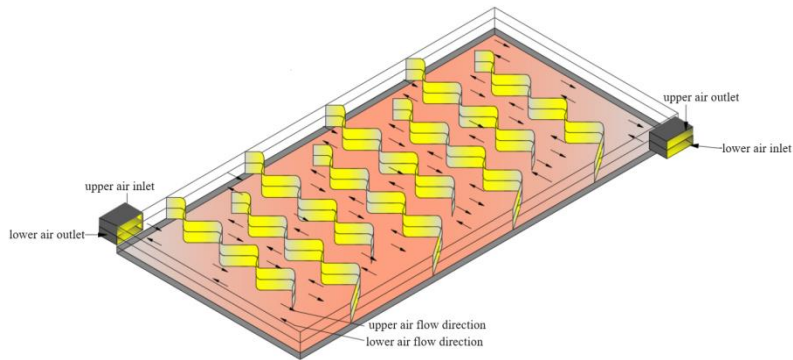
As the air inlet Reynolds number increases, the air outlet temperature decreases, although this decrease becomes progressively smaller. Simultaneously, the heat collection efficiency of the collector shows a gradual increase, although the rate of increase diminishes. On the other hand, the pressure loss of the collector exhibits a gradual increase, and this increase also grows progressively. This trend of change is consistent with reference [31], indicating the accuracy and reliability of the calculation. The pressure loss data is fitted using the curve fitting method, resulting in a square deviation of 0.997. This level of data deviation confirms the accuracy of the data fitting curve. The curve fitting illustrates a nonlinear functional relationship between the pressure loss and the inlet Reynolds number.

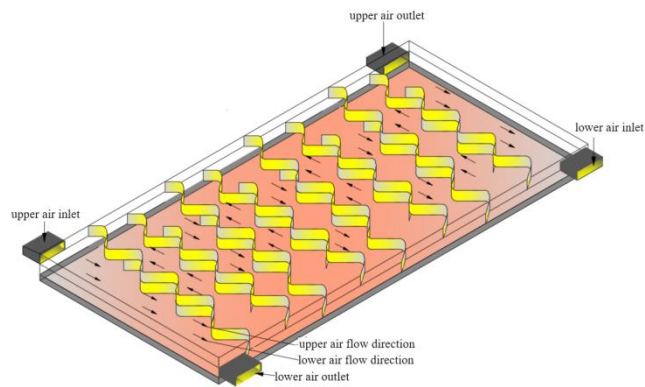## 4. Study on double-layer SAH with sinusoidal baffles

According to the previous research, when the air inlet flow of the SAH increases, the air outlet temperature will decrease, although the corresponding heat collection efficiency will increase. On this basis, the heat collection performance of the double-layer SAH with sinusoidal baffles is studied. In the double-layer collector, there are two air inlets and outlets; therefore, four kinds of double-layer SAH are set according to the different inlets and outlets, which are named the downstream same inlet (DSI), the downstream different inlet (DDI), the cross same inlet (CSI), and the cross different inlet (CDI). The upper and lower air inlets of the DSI are on the same side as the air outlets. The upper and lower air inlets and outlets of the DDI are located diagonally. The upper and lower air inlets of the CSI are parallel to the air outlets. The upper and lower air inlets of the CDI are distributed in opposition to the air outlets.
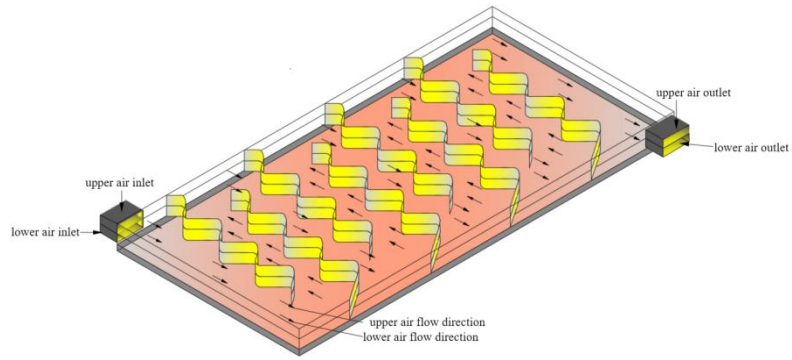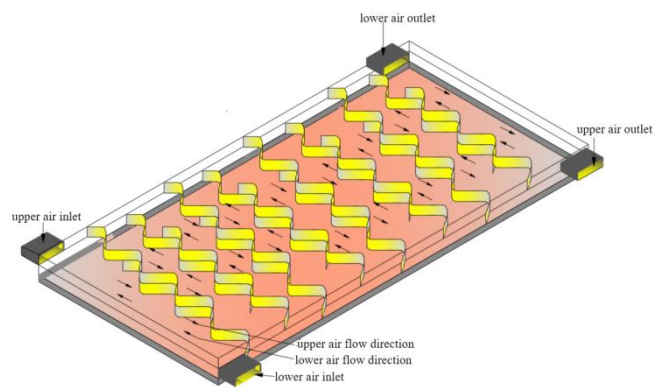
(a) DSI

(b) DDI

(c) CSI

(d) CDI

Figure 11. Model of double-layer SAH with sinusoidal baffles.

The air inlet Reynolds number is 0.57×10^4, the air inlet temperature is 278 K, and the ambient temperature is 274 K; these are used to calculate and study four kinds of double-layer SAH with sinusoidal baffles. The calculated data results are shown in Table 5.
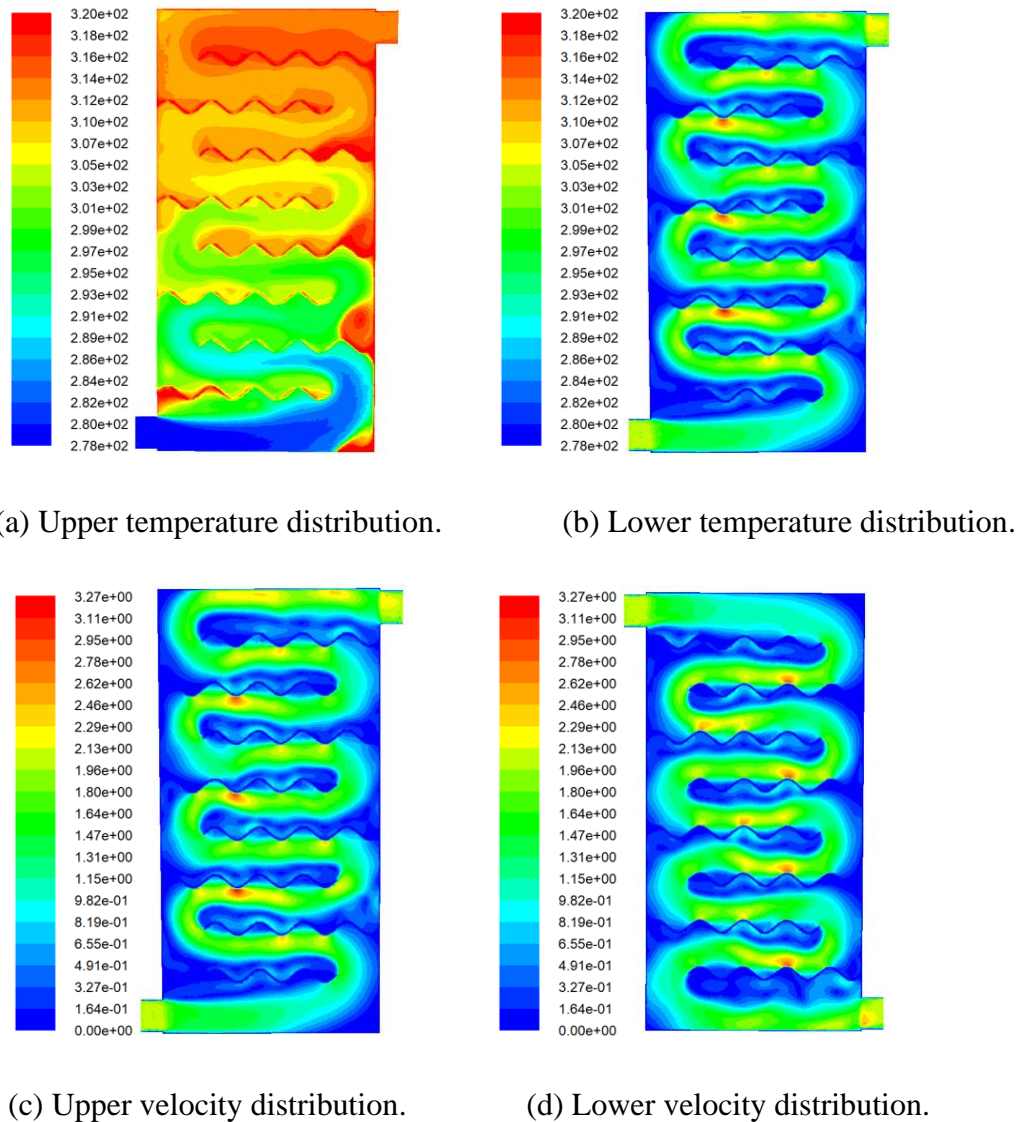
Table 5. Calculation data of four kinds of double-layer SAH.

Inlet type	Upper outlet temperature/K	Lower outlet temperature/K	Heat collection efficiency/%
DSI	314.29	315.9	73.41
DDI	313.02	317.70	73.94
CSI	313.44	316.21	72.88
CDI	314.87	318.59	76.63

Table 5 presents the comparison of data results, where the CDI exhibits the highest heat collection efficiency and outlet temperature, while the CSI registers the lowest. This outcome is attributed to the distinct airflow patterns in the CDI. Both the upper and lower air enter the inlet from different directions. This design ensures that the air remains unaffected by the flow direction during the entire process, allowing it to fully absorb heat from the heat absorption plate and the baffle. Consequently, the CDI achieves the most effective air heating.

When examining the calculation results for the DSI and the CSI, it becomes evident that the DSI model results in slightly lower outlet temperatures for the upper air. The DSI model has the same airflow direction for the upper and lower air, along with identical baffle arrangements in both layers, thus causing reduced heat gain for the lower air. On the other hand, the CSI model introduces a difference in the baffle arrangement sequence between the upper and lower layers. As the result, some of the heat from the heat absorption plate is absorbed by the baffle. Furthermore, the flow of the lower layer air reduces the heat gain of the upper layer air. These factors contribute to a decrease in the outlet temperatures of both the DSI and the CSI.

Upon analyzing the calculations for the DDI and the CDI, it becomes evident that the baffle arrangements and the heating order for cold air in the upper and lower layers differ between these two models. In the DDI model, the heat at a distance from the wall cannot be fully utilized, resulting in an inadequate heat absorption. In contrast, due to different air flow directions, the CDI model ensures that the flow of cold air in the upper and lower layers does not interfere with one another. Consequently, the cold air can efficiently absorb heat from the heat absorption plate and the baffle. These factors lead to the higher air outlet temperature in the CDI model. From this, it can be seen that using the CDI model in the double-layer sinusoidal baffle SAH not only achieves a high heat utilization, but also makes the outlet temperature suitable for indoor air heating in the winter.

(a) Upper temperature distribution.

(b) Lower temperature distribution.

(c) Upper velocity distribution.

(d) Lower velocity distribution.

Figure 12. Temperature and velocity distribution of CDI.

5. Conclusions and expectation

The research in this article is based on the folded baffle and semi-circular baffle SAH, aiming to improve the collection efficiency of the SAH and reduce the internal pressure loss of air, thus proposing a sinusoidal baffle SAH. Using Fluent to simulate the sinusoidal baffle SAH, this SAH was compared with the folded baffle and semi-circular baffle SAH, demonstrating the advantages of the sinusoidal baffle SAH. The wavelength, wave height, and air Reynolds number of the sinusoidal baffle were studied and analyzed, and the optimal wavelength, wave height, and Reynolds number were selected. The air inlet method of the double-layer sine baffle SAH were researched and analyzed, and the optimal air inlet method was studied. The specific conclusions obtained are as follows:

(1) Compared with the folded-baffles SAH, the SAH with sinusoidal baffles had a better heat performance; compared with semicircular baffles, the SAH with sinusoidal baffles not only had a lower pressure loss, but also had a higher heat collection efficiency.

(2) When the wavelength and wave height of sinusoidal baffles were in a small range, there was

little difference between the pressure loss and the heat collection effect. When the wavelength of the sinusoidal baffles was 200 mm, the heat collection effect was the best, and the heat collection efficiency was 64.49%; when the wave height was 30 mm, the maximum heat collection efficiency was 64.91% and the minimum pressure loss was 17.51 Pa.

(3) The air inlet Reynolds number had the greatest influence on the heat collection performance of the collector. The variation range of the air outlet temperature and the heat collection efficiency gradually decreased with the increase of Reynolds number, and the variation of pressure loss would gradually increase.

(4) Compared with the other three double-layer SAH with sinusoidal baffles, the CDI had the best heat collection performance. The upper outlet temperature was 314.87 K, the lower outlet temperature was 318.57 K, and the heat collection efficiency of the collector was 76.63%. The CDI model was beneficial for indoor heating in the winter.

In this paper, through research on the heat collection performance of a sinusoidal baffle collector, it is concluded that the heat collection performance of a sinusoidal baffle collector is better than that of a folded baffle collector and a semicircular baffle collector, which can ensure a high heat collection efficiency and reduce the pressure loss at the same time. However, there are also corresponding problems in the research.

a. The longitude, latitude, and solar radiation time in this paper were fixed values. When the parameters change, the calculation results will be affected.

b. The ambient temperature in the research hypothesis was constant, which did not rule out the change of ambient temperature caused by heat dissipation from the collector to the outside in the actual experimental process.

In the process of studying the double-layer sinusoidal baffle collector, this paper only studies one kind of air inlet Reynolds number. In future research works, we hope to study the influence of different inlet Reynolds numbers of the upper and lower layers on the heat collection performance of the double-layer collector. In addition, in the research hypothesis of this paper, the convective heat transfer between the PC cover plate and the outside world was ignored, and there was only radiation heat transfer with the outside world. In future research works, the overall heat dissipation of the collector can be calculated, which makes the calculation results of the heat collection performance of the sinusoidal baffle collector more accurate.

Use of AI tools declaration

Acknowledges

Author contributions

Xiaolong Wang is responsible for writing the paper; Lingning Zhang is responsible for editing the language and grammar of the manuscript; Yuan Chang is responsible for organizing and editing

the images in the manuscript; Yang Song made significant contributions to the revision of the manuscript; Liang Wang proposed innovative points for manuscript research and was responsible for the simulation calculations of the manuscript research

Conflict of interest

The authors declare that they have no known competing financial interest or personal relationships that could have appeared to influence the work reported in this paper.

References

1. Jia B, Liu F, Wang D (2019) Experimental study on the performance of spiral solar air heater. *Sol Energy* 182: 16–21. https://doi.org/10.1016/j.solener.2019.02.033

2. Hao W, Zhang H, Liu S, et al. (2012) Design and prediction method of dual working medium solar energy drying system. *Appl Therm Eng* 195: 117153. https://doi.org/10.1016/j.applthermaleng.2021.117153

3. Zayed ME, Zhao J, Elsheikh AH, et al. (2019) Application of cascaded phase change materials in solar water collector storage tank:A review. *Sol Energy Mater Sol Cells* 199: 24–49. https://doi.org/10.1016/j.solmat.2019.04.018

4. Yin Y, Chen H, Zhao X, et al. (2022) Solar-absorbing energy storage materials demonstrating superior solar-thermal conversion and solar-persistent luminescence conversion towards building thermal management and passive illumination. *Energy Convers Manage* 266: 115804. https://doi.org/10.1016/j.enconman.2022.115804

5. Muthukumaran J, Senthil R (2022) Experimental performance of a solar air heater using straight and spiral absorber tubes with thermal energy storage. *J Energy Storage* 45: 103796. https://doi.org/10.1016/j.est.2021.103796

6. Stelian BA, Croitoru C, Bode F, et al. (2022) Experimental investigation of an enhanced transpired air solar collector with embodied phase changing materials. *J Cleaner Prod* 336: 130398. https://doi.org/10.1016/j.jclepro.2022.130398

7. Zayed ME, Zhao J, Li W, et al. (2020) Recent progress in phase change materials storage containers: Geometries, design considerations and heat transfer improvement methods. *J Energy Storage* 30: 101341. https://doi.org/10.1016/j.est.2020.101341

8. El-Said EMS, Gohar MA, Ali A, et al. (2022) Performance enhancement of a double pass solar air heater by using curved reflector: Experimental investigation. *Appl Therm Eng* 202: 117867. https://doi.org/10.1016/j.applthermaleng.2021.117867

9. Heydari A, Mesgarpour M (2018) Experimental analysis and numerical modeling of solar air heater with helical flow path. *Sol Energy* 162: 278–288. https://doi.org/10.1016/j.solener.2018.01.030

10. Gopi R, Ponnusamy P, Fantin AA, et al. (2021) Performance comparison of flat plate collectors in solar air heater by theoretical and computational method. *Mater Today: Proc* 39: 823–826. https://doi.org/10.1016/j.matpr.2020.09.809

11. Nain S, Ahlawat V, Kajal S, et al. (2021) Performance analysis of different U-shaped heat exchangers in parabolic trough solar collector for air heating applications. *Case Stud Therm Eng* 25: 100949. https://doi.org/10.1016/j.csite.2021.100949

12. Perwez A, Kumar R (2019) Thermal performance investigation of the flat and spherical dimple absorber plate solar air heaters. *Sol Energy* 193: 309–323. https://doi.org/10.1016/j.solener.2019.09.066

13. Jiang Y, Zhang H, Wang Y, et al. (2021) A comparative study on the performance of a novel triangular solar air collector with tilted transparent cover plate. *Sol Energy* 227: 224–235. https://doi.org/10.1016/j.solener.2021.08.083

14. Zhang H, Ma X, You S, et al. (2018) Mathematical modeling and performance analysis of a SAH with silt-perforated corrugated plate. *Sol Energy* 167: 147–157. https://doi.org/10.1016/j.solener.2018.04.003

15. Saedodin S, Zaboli M, Ajarostaghi SSM (2021) Hydrothermal analysis of heat transfer and thermal performance characteristics in a parabolic trough solar collector with Turbulence-Inducing elements. *Sustainable Energy Technol Assess* 46: 101266. https://doi.org/10.1016/j.seta.2021.101266

16. Chand S, Chand P, Kumar GH (2022) Thermal performance enhancement of solar air heater using louvered fins collector. *Sol Energy* 239: 10–24. https://doi.org/10.1016/j.solener.2022.04.046

17. Rehman T, Nguyen DD, Sajawal M (2024) Smart optimization and investigation of a PCMs-filled helical finned-tubes double-pass solar air heater: An experimental data-driven deep learning approach. *Therm Sci Eng Prog* 49: 102433. https://doi.org/10.1016/j.tsep.2024.102433

18. Saravanakumar PT, Somasundaram D, Matheswaran MM (2020) Exergetic investigation and optimization of arc shaped rib roughened solar air heater integrated with fins and baffles. *Appl Therm Eng* 175: 115316. https://doi.org/10.1016/j.applthermaleng.2020.115316

19. Marwa A, Ameni M, Hatem M, et al. (2020) Numerical analysis of SAH provided with rows of rectangular fins. *Energy Rep* 6: 3412–3424. https://doi.org/10.1016/j.egyr.2020.11.252

20. Aref L, Fallahzadeh R, Shabanian SR, et al. (2021) A novel dual-diameter closed-loop pulsating heat pipe for a flat plate solar collector. *Energy* 230: 120751. https://doi.org/10.1016/j.energy.2021.120751

21. Saravanan A, Murugan M, Sreenivasa RM, et al. (2021) Thermo-hydraulic performance of a solar air heater with staggered C-shape finned absorber plate. *Int J Therm Sci* 2021, 168: 107068. https://doi.org/10.1016/j.ijthermalsci.2021.107068

22. Du J, Chen H, Li Q, et al. (2024) Turbulent flow-thermal-thermodynamic characteristics of a solar air heater with spiral fins. Int J Heat Mass Transfer 226: 125434. https://doi.org/10.1016/j.ijheatmasstransfer.2024.125434

23. Elumalai V, Arunkumar T, Thiruselvam K, et al. (2021) Thermal performance improvement in solar air heating: An absorber with continuous and discrete tubular and v-corrugated fins. *Therm Sci Eng Prog* 48: 102416. https://doi.org/10.1016/j.tsep.2024.102416

24. Waheed S, Mahamed E, Ravishankar S, et al. (2023) Performance evaluation of a solar air heater with staggered/longitudinal finned absorber plate integrated with aluminium sponge porous medium. *J Build Eng* 73: 106841. https://doi.org/10.1016/j.jobe.2023.106841

25. Wang L, Man Y (2018) Numerical simulation of SAH with folded baffles. *Renewable Energy Resour* 36: 997–1003. https://doi.org/10.13941/j.cnki.21-1469/tk.2018.07.008

26. Jia B, Yang L, Zhang L, et al. (2021) Optimizing structure of baffles on thermal performance of spiral solar air heaters. *Sol Energy* 224: 757–764. https://doi.org/10.1016/j.solener.2021.06.043

27. Rani P, Tripathy PP (2022) Experimental investigation on heat transfer performance of solar collector with baffles and semicircular loops fins under varied air mass flow rates. *Int J Therm Sci* 178: 107597. https://doi.org/10.1016/j.ijthermalsci.2022.107597

28. Jia B, Liu F, Li X, et al. (2021) Influence on thermal performance of spiral solar air heater with longitudinal baffles. *Sol Energy* 225: 969–977. https://doi.org/10.1016/j.solener.2021.08.004

29. Zayed ME, Kabeel A, Bashar S, et al. (2023) Performance augmentation and machine learning-based modeling of wavy corrugated solar air collector embedded with thermal energy storage: Support vector machine combined with Monte Carlo simulation. *J Energy Storage* 74: 109533. https://doi.org/10.1016/j.est.2023.109533

30. Magda K, Aly-Eldeen A, Abdelmaqsoud A, et al. (2024) Enhanced performance assessment of an integrated evacuated tube and flat plate collector solar air heater with thermal storage material. *Appl Therm Eng* 245: 122653. https://doi.org/10.1016/j.applthermaleng.2024.122653

31. Wang L (2022) Research on the collect heat performance of new type collector. *Energy Sources, Part A: Recovery, Util, Environ Effects*, 44: 9412–9427. https://doi.org/10.1080/15567036.2021.1954729

32. Song Z, Xue Y, Jia B, et al. (2022) Introduction of the rectangular hole plate in favor the performance of photovoltaic thermal solar air heaters with baffles. *Appl Therm Eng* 220: 119774. https://doi.org/10.1016/j.applthermaleng.2022.119774

33. Zhang D, Zhang J, Zhang Y, et al, (2019) Baffles optimization of a flat plate SAH with double channel. *J Shanghai Jiao tong Univ* 53: 1302–1307. https://doi.org/10.16183/j.cnki.jsjtu.2019.11.005